CIMAC CONGRESS 25
ZURICH, MAY 19 – 23, 2025

2025 | 045

Hydrogen in Large-Bore Engine Applications: Insights on Experimental and Simulative Research

Fuels - Alternative & New Fuels

Andreas Zepf, Technical University of Munich, Institute of Sustainable Mobile Powertrains

Felina Armbruster, Technical University of Munich, Institute of Sustainable Mobile Powertrains
Maximilian Prager, Technical University of Munich, Institute of Sustainable Mobile Powertrains
Malte Jaensch, Technical University of Munich, Institute of Sustainable Mobile Powertrains

DOI: https://doi.org/10.5281/zenodo.15195504

ABSTRACT

The transition of large-bore engines from fossil fuels to hydrogen demands significant adaptations due to hydrogen’s unique properties. These adaptations encompass modifications to engine components and operating strategies to ensure efficient and reliable performance. At the Technical University of Munich, experimental and simulative studies on a 4.77 L single-cylinder engine aim to advance hydrogen’s role in stationary and mobile large-scale applications. This study, therefore, explores four key research areas, combining experimental and simulative investigations. First, reaction mechanisms for hydrogen combustion simulation are compared to accurately depict hydrogen combustion. Among the four reaction mechanisms evaluated (Conv 3.0, Nordin, GRI 3.0, Burke-2012), Conv 3.0 demonstrates the highest accuracy with minimal deviations, making it the most suitable for further investigation. Second, investigations on gaseous emissions in hydrogen versus natural gas operation are performed. Hydrogen operation yields negligible carbon emissions but significant NOx emissions, increasing with richer fuel mixtures from 12.0 ppm at AFR = 2.8 to 185.5 ppm at AFR = 2.3, driven by hydrogen's high flame temperature. Third, particulate emissions are evaluated for hydrogen and natural gas. Particle emissions range from 10e4 to 10e5 #/cm³ for both hydrogen and natural gas, with slightly higher levels in hydrogen operation due to increased lubrication oil influence. Fourth, the influence of higher exhaust back pressures, which typically occur on turbocharged engines, on hydrogen combustion is investigated. Elevated exhaust back pressure prolongs combustion duration, decreases efficiency, and increases residual gas content. To address these challenges, innovative turbocharger designs – such as electric or mechanically decoupled systems – are proposed to mitigate back pressure and enhance efficiency, paving the way for hydrogen as a competitive alternative fuel.

1 INTRODUCTION

Efforts to achieve global decarbonization motivate the development of new technologies across various sectors, including transportation, energy production, and industry [1]. Despite the growing momentum of electrification in the transportation sector, particularly for passenger vehicles [2, 3], the unique demands of the maritime and energy industries present significant barriers to full electrification. Given the limited energy density of current battery technology, the electrification of applications within the marine and energy sectors remains challenging [4]. Furthermore, the inherent intermittency of renewable energy sources, such as solar and wind power, introduces uncertainties in availability, posing a significant obstacle for these sectors, which require reliable and consistent power supply [4]. To mitigate the challenges of intermittent renewable energy sources, Power-to-Gas technologies offer a promising solution. These concepts involve converting excess renewable electricity into storable gases like hydrogen, enabling on-demand utilization or reconversion back to electricity [4–6]. Figure 1 shows a concept whereby energy surplus from renewable energies is stored in hydrogen and can either be reconverted to electricity or used in mobile or stationary applications. Replacing fossil fuels with hydrogen, these applications can achieve CO_2-neutral operation.

Despite the cost-efficiency advantages of gas turbines, hydrogen internal combustion engines (H2ICE) offer a compelling alternative [7]. Leveraging advancements from automotive research, market-ready H2ICE-based combined heat and power (CHP) plants provide operational flexibility, accommodating rapid load changes and demonstrating strong part-load performance [7–10]. This makes them well-suited for grid stabilization and peak load coverage [7, 10, 11]. Furthermore, their decentralized deployment potential reduces transmission losses and enhances grid security [7]. Integration into CHP plants maximizes overall efficiency, with potential revenue streams from electricity and heat generation up to a combined efficiency of 90 % [7, 12].

As the Power-to-H_2 infrastructure continues to evolve, significant strides have been made in developing high-efficiency, large-scale H2ICEs. Progress from 2021 to 2024 highlights a clear trajectory toward full hydrogen integration. One key development task for hydrogen operation is achieving the same power density and efficiency as current large-scale natural gas CHP systems, with outputs of up to 2.5 MW [13–17]. Experimental and simulative studies are being conducted at the Institute of Sustainable Mobile Powertrains at the Technical University of Munich to support the ongoing advancements in hydrogen engine technology. This study presents an overview of the current research focus and highlights the cooperation between experimental results and computational simulations. The focus of this study lies in four key areas. First, reaction kinematics for hydrogen combustion are evaluated to ensure accurate modeling in 3D computational fluid dynamic (CFD) simulations, enabling a deeper understanding of combustion behavior. Second, exhaust gas emissions – including NO_x, total hydrocarbons (THC), CO_2, and hydrogen – are analyzed under variations of air-fuel ratio (AFR, λ) and engine load (indicated mean effective pressure, IMEP) for both natural gas and hydrogen operation. Third, particle emissions are investigated under motored, natural gas, and hydrogen combustion conditions, again considering changes in AFR and IMEP. Finally, the study examines exhaust gas turbocharging, focusing on exhaust gas temperatures (EGT), enthalpies, and the impact of back pressure on engine operation.

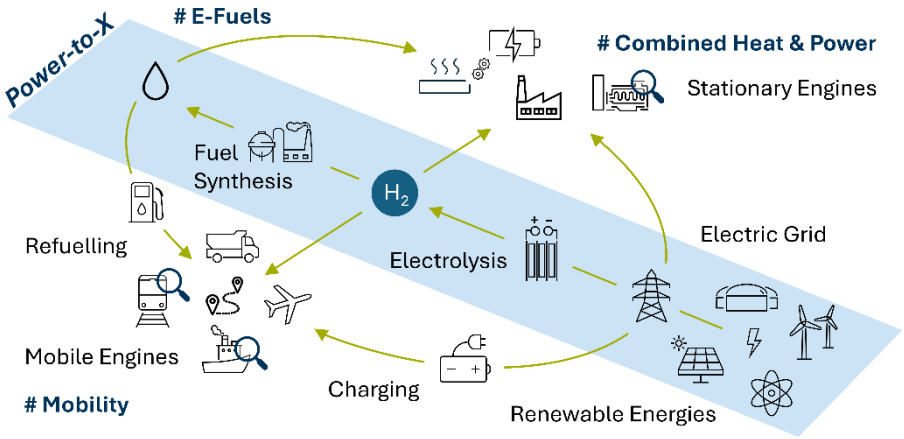

Figure 1: Overview on a Power-to-X concept, depicting a Power-to-H_2 strategy

Combining experimental data with simulation insights, this work aims to identify key opportunities for optimizing hydrogen engine performance and emissions, contributing to developing more efficient and sustainable combustion systems.

2 TEST BENCH SETUP

Experiments are conducted on a single-cylinder research engine derived from a large-scale gas engine typically used for power generation and marine applications (specifications in Table 1). The test bench enables control of charge air conditions, including temperature, humidity, and pressure (up to 10 bar and 1000 kg/h mass flow). Intake air humidity is controlled by adding saturated steam from softened water to the charged air. A light Miller inlet valve timing is used for the valve timing. For ignition, an unscavenged pre-chamber spark plug is utilized. The spark plug electrode material was modified to mitigate the risk of combustion anomalies associated with hydrogen operation. This modification is necessary because hydrogen's wider flammability limits and faster flame speed increase the risk for pre-ignition, knocking, and even backfire with a standard gas-engine spark plug. The engine's compression ratio is adjustable. This is achieved by modifying the cylinder housing position, effectively altering the clearance volume between the piston and cylinder head at the top dead center (TDC). This flexibility allows for investigating the effects of compression ratio on engine performance and emissions under different operating conditions. A piezoelectric pressure sensor (AVL GU21D), integrated into the cylinder head, provides high-resolution pressure measurements with a sampling precision of up to 0.05 °CA (crank angle degree). Piezoresistive sensors in both the inlet and exhaust manifolds and multiple pressure transmitters and thermocouples throughout the engine enable precise monitoring of operational parameters for thermodynamic analysis.

The hydrogen sourced from bundles of 300 bar with a quality of 3.0 is added to the charge air through a venturi mixer. Subsequently, the fuel-air mixture is homogenized within the intake manifold prior to entering the engine. This ensures a uniform mixture and consistent combustion within the cylinder. For lubrication, Sentron LD 8000 by Petro-Canada Lubricants was selected. This low-ash (0.52 wt%) engine oil, with a sulfur content of 0.288 wt%, was chosen to minimize ash deposits and potential interactions with the combustion process, particularly during hydrogen operation [18, 19]. The exhaust gas line has temperature and pressure sensors immediately downstream of the cylinder head outlet ports.

Table 1. Single-cylinder engine specification and operations conditions

Specifications	Values and details
Bore	170 mm
Stroke	210 mm
Displacement	4.77 l
Compression ratio	11.65
Valves	2 inlet and 2 outlet valves
Valve timing	Light Miller valve timing
Ignition system	Pre-chamber spark plugs
Injection system	PFI
Turbocharger emulation	Exhaust throttle with charger efficiency control
Start of injection	80°CA bTDC
Inlet pressure gas	7 bar
Engine oil	Sentron LD 8000

2.1 Exhaust Gas Measurement Setup

A Horiba MEXA-ONE D1 gas analyzer, connected downstream of these sensors, measures gaseous emissions, including CO_2, CO, THC, and NO_x. A V&F HSense is also integrated into the exhaust line for hydrogen slip measurement through Electron Ionization Mass Spectroscopy.

2.2 Particle Measurement Setup

Particle number concentrations are measured using a Horiba Solid Particle Counting System 2300, featuring a Condensation Particle Counter (CPC) with a 50 % cut-off size of 23 nm. A TSI Inc. Model 3772 CPC (50 % cut-off at 10 nm) was integrated to enhance measurement capabilities, enabling synchronous measurement of smaller particles. A catalytic stripper operating at 350 °C removed volatile compounds and prevented their interference with particle counting. The system incorporates a dilution system with a total dilution ratio of 1:1500 to avoid overloading the catalytic stripper and ensure accurate particle counting. Measured concentrations were corrected for dilution and represented the actual particle concentrations in the exhaust gas. The particle counting system was positioned downstream of the exhaust throttle to avoid exposure to high pressures. [4, 20]

3 SIMULATION SETUP

CFD simulations were performed to complement the experimental investigations and gain a deeper understanding of the in-cylinder processes. The simulations aimed to provide insights into the combustion behavior of hydrogen, including flame propagation, temperature distribution, and species formation. The CONVERGE [21] software package

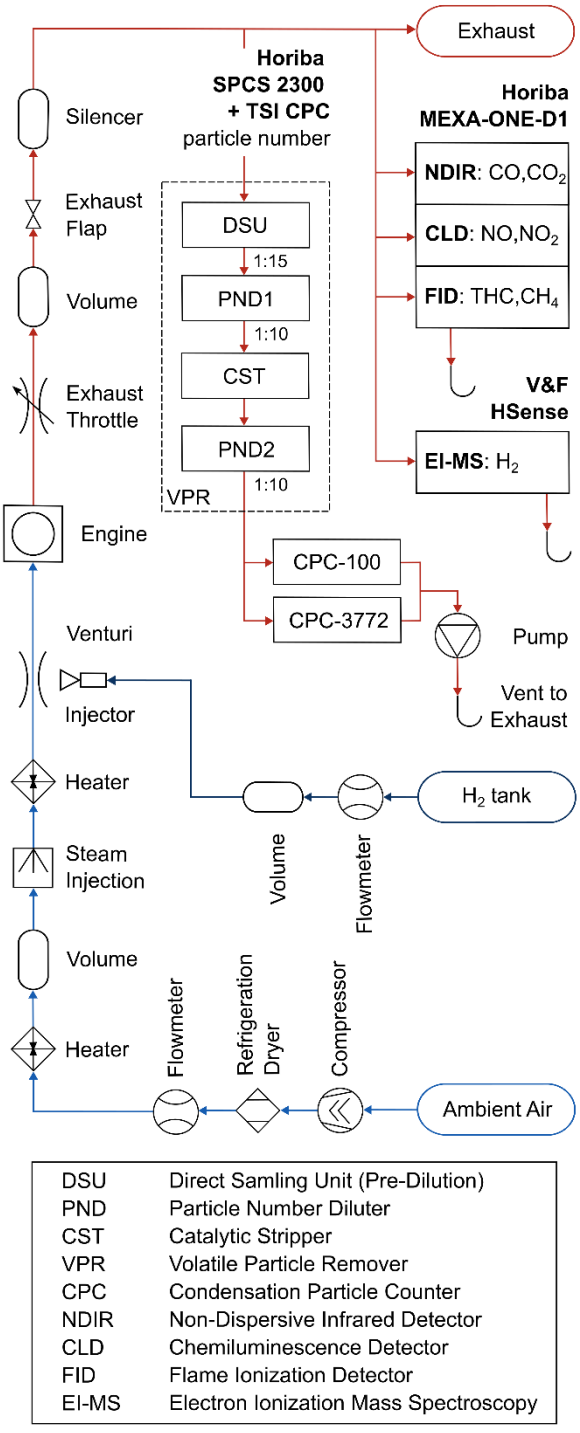

Figure 2: Overview of the test bench and exhaust gas measurement setup

was utilized to create a detailed engine model. This model employed the Standard k-ε Reynolds-Averaged Navier-Stokes turbulence model and the SAGE detailed chemistry solver [22] to accurately represent the turbulent flow and combustion chemistry. CONVERGE's meshing strategy combines a modified cut-cell Cartesian method with Adaptive Mesh Refinement [23]. The cut-cell approach generates an orthogonal grid, simplifying the meshing process. The Adaptive Mesh Refinement dynamically refines the mesh in areas of high gradients or complex flow features, ensuring accurate resolution of critical flow structures [23]. This adaptive refinement eliminates predefining regions requiring a finer mesh, allowing for a more efficient and automated workflow [23]. In CONVERGE, the base grid cell size determines the initial mesh resolution. Mesh refinement is achieved through the embed scale parameter, which can be used for fixed embedding (a priori refinement) or adaptive embedding with Adaptive Mesh Refinement. Fixed embedding refines the mesh in specified regions throughout the simulation, while Adaptive Mesh Refinement dynamically refines the mesh based on criteria such as velocity gradients or species concentrations. The cell size of the refined mesh is given by:

$$\mathrm{dx} = \mathrm{dx}_{\mathrm{base}} \cdot 2^{-(\mathrm{embed\ scale})} \qquad (1).$$

A base grid size of 20 mm was used in this study. The resulting cell sizes, obtained through the application of Adaptive Mesh Refinement and fixed embedding, are presented in Table 2.

Table 2. Cell sizes of different regions

Region	Initial cell size	Minimum cell size
Intake manifold	5 mm	0.625 mm
Combustion chamber	5 mm	0.3125 mm
Exhaust manifold	5 mm	0.625 mm

CONVERGE employs the finite volume method to solve the conservation equations, with all solution variables stored at the cell centers. This cell-centered approach ensures an accurate representation of the flow field. The pressure-velocity coupling is handled using the Pressure Implicit with Splitting of Operators (PISO) method of Issa [24], which offers improved accuracy and stability compared to more straightforward methods. A variable time-stepping scheme is employed to adjust the time step size based on the flow conditions, ensuring accuracy and computational efficiency. The pressure and temperature boundary conditions for the in- and outlet were obtained from experimental results. The pressure type is set to static for both the intake and the outflow boundary. The temperatures for the wall boundaries of the intake and exhaust manifold and the liner wall boundary are set as the coolant temperature in the experiment of 90 °C. The piston and exhaust valve wall temperatures are also set to 90 °C for the model validation via a load exchange simulation. For the combustion simulation, the

piston and exhaust valve wall temperature are assumed to be higher and set to 250 °C. The valve timings of the test bench setup are implemented. CONVERGE uses an event-based approach to simulate valve motion. This involves cyclically disconnecting the intake and exhaust manifolds based on the valve timing, effectively delimiting the individual regions and preventing mass exchange between them. To accurately capture the compression ratio, the model accounts for the compression of the cylinder head gasket. This is achieved by performing non-reacting simulations with varying compression ratios and comparing the resulting mass flow rate and in-cylinder pressure with experimental data. The compression ratio in the model is then adjusted until the simulation results match the experimental measurements. Figure 3 shows the resulting in-cylinder pressure for the validated model and the deviation from the experimental measurements. The close agreement between the simulated and experimental pressures with a maximum deviation of 2.5 % demonstrates the model's accuracy in capturing the engine's thermodynamic behavior.

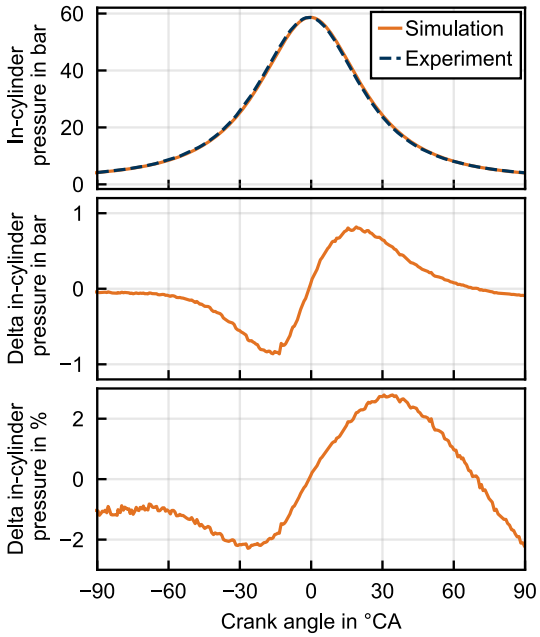

Figure 3: In-cylinder pressure and deviation between simulation and experiment

4 REACTION KINEMATICS

Precise chemical modeling is necessary to accurately depict hydrogen's combustion mechanisms and specific combustion characteristics [25, 26]. The H_2/O_2 mechanism is not only relevant for hydrogen combustion but also for the combustion of fossil fuels [27]. Hydrocarbons also require the species and reactions included in the H_2/O_2 mechanism [27]. This commonality allows the establishment of H_2/O_2 reaction mechanisms to be used as a basis for modeling more complex hydrocarbon combustion processes [27]. Several H_2/O_2 mechanisms have been validated against thermodynamic measurements, including those by Ó Conaire et al. [28] and Li et al. [29], which build upon the mechanism by Müller et al. [30]. In addition to H_2/O_2 mechanisms, sub-mechanisms for H_2/CO reactions are also available, such as the GRI 3.0 mechanism [31], which was extended by Davis et al. [32] to include third-body reactions and OH radicals:

$$H + O_2 + M \rightleftharpoons HO_2 + M \quad (2).$$

Saxena et al. [33] developed a detailed H_2/CO mechanism with fewer third-body reactions, featuring an initiation step for carbon monoxide formation instead of hydrogen. Konnov [34] considered the reaction rate between hydrogen atoms and HO_2 radicals, the pressure dependence of HO_2 radical recombination, and the reaction rate between OH and HO_2 radicals. Burke et al. [35] extended the Li et al. [29] mechanism to high-pressure, low-temperature conditions by incorporating pressure and temperature dependence of the HO_2 reaction rate. Hong et al. [36] updated the mechanism with new reaction rate parameters for $H+O_2$, the reverse reaction of H_2O_2, and pressurized, heated H_2O/O_2 mixtures. Kéromnes et al. [26] highlighted the importance of specific reaction pathways (Eq. 3, Eq. 4) for predicting ignition delay at moderate to high temperatures. In contrast, chain reactions at low temperatures and pressures (Eq. 5, Eq. 6) involving HO_2 and OH radicals dominate flame zone reactivity. Varga et al. [37] optimized this mechanism for ignition delay and flame speed, resulting in an optimized 11-step mechanism deemed most suitable for their study.

$$H_2 + HO_2 \rightleftharpoons H + H_2O_2 \quad (3).$$

$$H_2O_2 + (M) \rightleftharpoons 2OH + (M) \quad (4).$$

$$H + O_2 \rightleftharpoons O + OH \quad (5).$$

$$H + O_2 + (M) \rightleftharpoons HO_2 + (M) \quad (6).$$

Four reaction mechanisms were selected to evaluate their performance in simulating hydrogen combustion (Table 3). CONVERGE's default for hydrogen, Conv 3.0 [21], and the Burke-2012 [35] mechanism provide dedicated models for hydrogen combustion. The comparison included the well-

established GRI 3.0 [31] methane mechanism and the Nordin [38] n-heptane mechanism, commonly used as a diesel surrogate in CONVERGE, to assess the applicability of mechanisms developed for other fuels.

Table 3. Overview of reaction mechanisms investigated

Name	Ref.	Species	Reactions	CO_2	He	Ar
Conv 3.0	[21]	13	23	X	X	X
Burke-2012	[35]	9	20	-	-	-
GRI 3.0	[31]	53	325	X	X	X
Nordin	[38]	42	168	X	-	-

To evaluate the suitability of the different reaction mechanisms, the in-cylinder pressure, its deviation from experimental data, and the calculated heat release rate are compared in Figure 4. The comparison was conducted at an operating point taken from the experimental data, characterized by an IMEP of 19.7 bar, a center of combustion (CoC) at MFB50 (Mass Fraction Burned) = 9 °CA aTDC (after TDC), an AFR of λ = 2.3, an intake pressure of 3.6 bar absolute, an exhaust back pressure of 1.4 bar absolute, and an engine speed of 1500 rpm. To introduce the hydrogen with the correct AFR, the boundary and initial condition of the intake manifold are set to a homogenous mixture of air and hydrogen.

The different mechanisms represent combustion with varying degrees of accuracy. The Conv 3.0 and Nordin mechanisms show the best agreement in the cylinder pressure, each with an root mean square error (RMSE) of 1.09 bar over the entire cycle. Conv 3.0 shows a more significant relative deviation in peak pressure than Nordin. The latter also indicates a higher heat release rate than Conv 3.0. However, Nordin's ignition delay (MFB0-MFB5) is higher at 8.45 °CA than Conv 3.0 at 7.66 °CA. The similarity of the mechanisms is also evident in the temperature distribution shown in Figure 5. The temperatures at TDC and 12°CA aTDC hardly differ between the two mechanisms. Due to the shorter ignition delay, flame propagation with Conv 3.0 is already more advanced at TDC than with Nordin. Therefore, higher temperatures also appear with Conv 3.0 than with Nordin at 12 °CA bTDC. At 12 °CA aTDC, however, there are no discernible differences in flame propagation. This is caused by Nordin's higher maximum heat release rate than Conv 3.0. The higher ignition delay is compensated for in Nordin by a higher flame velocity with a higher heat release rate. Comparing the relative deviation from the experiment suggests that the real hydrogen combustion can be reproduced more accurately with the Conv 3.0 mechanism. At the same time, Nordin shows a higher deviation between the ignition and the maximum combustion chamber pressure. However, it is possible to reproduce the experimental results with both mechanisms.

The methane mechanism GRI 3.0 delivers similarly good results. With an RMSE of 2.0 bar and an ignition delay of 9.55 °CA, lower temperatures are reached in the combustion chamber during combustion. The flame propagation at TDC is less than that of Conv 3.0 and Nordin but is in a similar range. The relative deviation from the experimental cylinder pressure suggests that the ignition delay with GRI 3.0 is assumed to be too long. Like Nordin, this is offset during combustion by a higher flame speed with a higher heat release rate. GRI 3.0 shows the highest maximum heat release rate of all mechanisms investigated.

Burke-2012, on the other hand, massively overestimates the ignition delay at 17.56 °CA. This results in an RMSE of 7.0 bar due to the late start of combustion. As a result, the heat release rate is also lower than with the other mechanisms. The slower combustion becomes particularly clear in the temperature distribution in the combustion chamber. Here, a similar flame spread is only achieved at 12 °CA aTDC as with the other mechanisms at TDC. Therefore, it can be concluded that Burke-2012 is unsuitable for further investigations due to the excessive deviations from the experiment.

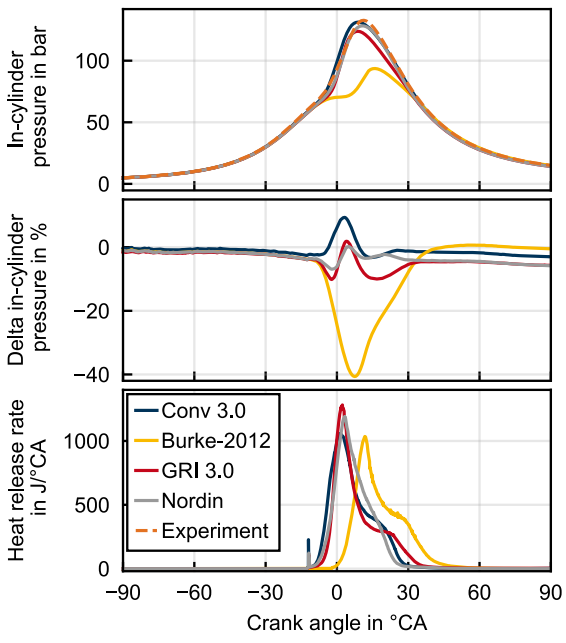

Figure 4: In-cylinder pressure, deviation from experiment, and heat release rate for different reaction mechanisms

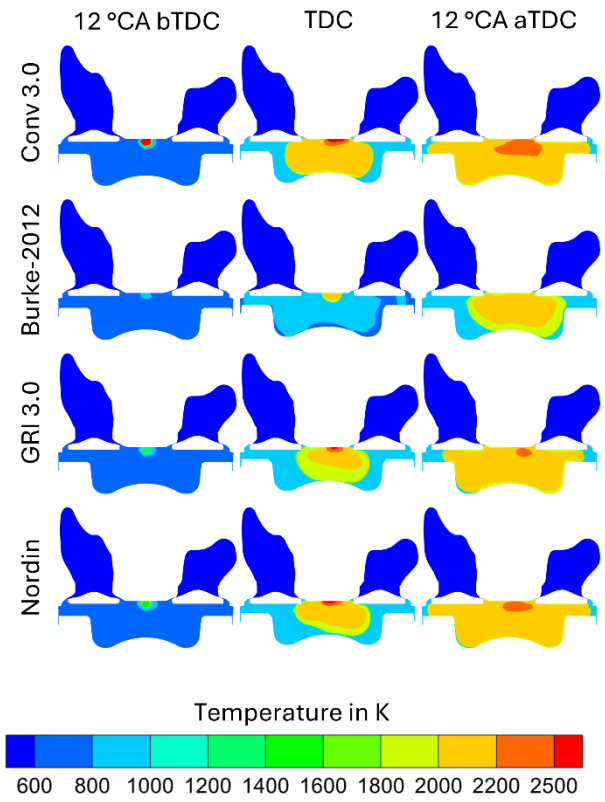

Figure 5: In-cylinder temperature distribution for different reaction mechanisms

Since Conv 3.0 with Nordin has the lowest RMSE and the lowest deviation in the cylinder pressure curve for assessing the ignition delay, the Conv 3.0 mechanism is used for further investigations in this work.

5 EXHAUST GAS MEASUREMENT

The combustion of hydrogen follows the reaction $H_2 + O_2 \rightarrow H_2O$, producing water as the primary product. However, under real combustion conditions, environmentally relevant emissions must be considered. Combustion with air results in the formation of NO_x, while incomplete combustion leads to hydrogen slip. Residual THC and particle emission can furthermore result from interactions with or co-combustion of engine lubrication oil [14, 20]. Figure 6 compares the mass fractions of raw exhaust gas compositions for different fuels. The most significant fraction in the exhaust gas is consistently nitrogen, reflecting its 75.5 wt% proportion in ambient air. Due to the over-stoichiometric combustion characteristic of diesel and hydrogen applications, the exhaust compositions contain a remaining share of residual oxygen.

In the following, the emission of THC, NO_x, CO_2, and the respective fuel slip, H_2 or rather CH_4, in hydrogen and natural gas operations are analyzed depending on varying AFR and IMEP. The AFR was adjusted in increments of 0.05, ranging from $\lambda = 1.3$ to 1.45 for natural gas, and in increments of 0.10, ranging from $\lambda = 2.3$ to 2.8 for hydrogen, while maintaining constant conditions for CoC and IMEP. A similar method is employed for IMEP variations, which range from 18 to 20 bar in 0.5-bar increments for natural gas and from 14 to 19 bar in 1.0-bar increments for hydrogen at a respective AFR of $\lambda = 1.4$ and $\lambda = 2.5$. The elevated load in natural gas operation results from operating on a consistently low compression ratio of 11.65, optimized for hydrogen operation, necessitating a higher load level to ensure stable natural gas combustion. The CoC was held at 15 °CA aTDC for natural gas and 10 °CA aTDC for hydrogen by adjusting the ignition timing. These CoC values were selected to ensure stable combustion across all variations for each fuel. The intake air was preconditioned to a temperature of 40 °C for natural gas operation. However, due to frequent backfire incidents under the same conditions with hydrogen, the intake air temperature was reduced to a constant 30 °C for hydrogen operation. [39]

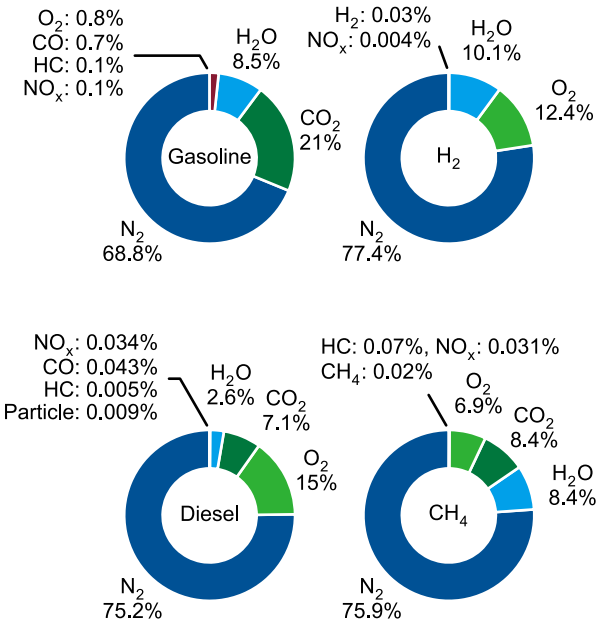

Figure 6: Typical raw exhaust gas compositions in wt% for gasoline, diesel, hydrogen, and natural gas. Data taken from Ref. [39, 40]

Figure 7 shows the influence of AFR and IMEP variation on NO_x, THC, CO, CO_2, and the respective fuel slip in hydrogen and natural gas operations. Due to the lack of fuel-dependent carbon, hydrogen operation produces minimal carbon exhaust gas emissions, as seen for THC, CO, and CO_2. THC and CO emission measurements fall within measuring uncertainty. CO_2 emissions in hydrogen operation show a

constant minimum of 500 ppm, likely due to ambient air. When considering compliance with the German TA Luft directive [40], which governs NO_x, THC, and CO emissions, the hydrogen engine solely registers significant emission values for NO_x. NO_x emissions significantly rise with richer fuel mixture from 12.0 ppm for an AFR of λ = 2.8 to 185.5 ppm for an AFR of λ = 2.3. With an average of 90.9 %, NO is predominant in NO_x, later oxidizing to NO_2. The peak NO_x emissions are equivalent to 794.6 mg/m³, momentarily surpassing the 500 mg/m³ limit. Higher NO_x emissions for richer mixtures result from hydrogen's high adiabatic flame temperature and the rising peak temperatures in the cylinder. The high laminar flame speed of hydrogen up to 185 cm/s (methane: 38 cm/s) leads to high combustion efficiencies, as the combustion process closely resembles the ideal thermodynamic Otto cycle. This results in an average indicated efficiency of 42.3 % in natural gas and 46.8 % in hydrogen operation. The relatively low efficiency compared to state-of-the-art lean burn gas engines in natural gas operation stems from the constant low compression ratio, necessitating a late combustion phasing for a stable combustion process. Therefore, the resulting statements for natural gas operations should only be seen as general tendencies. Hydrogen's high flammability results furthermore in improved lean running conditions and rather modest requirements regarding homogeneous mixture formation, even in very lean combustion conditions. Meanwhile, leaner combustion favors hydrogen slip, rising to 1297 ppm for an AFR of λ = 2.75. Variations of the IMEP lead to a decrease of 67 ppm hydrogen per +1-bar increment in IMEP due to more stable combustion. [39–45]

In contrast to hydrogen operation, natural gas operation with its combustion-bound CO_2 formation results in 71,150 ppm for an AFR of λ = 1.4, rising to 80,170 ppm for an AFR of λ = 1.3, equivalent to approximately 6,000 ppm per -0.1 AFR. At the same time, CO_2 emissions remain unchanged across variations in IMEP. THC emissions conversely increase with leaner combustion as incomplete combustion occurs, resulting equally in higher CO emissions of up to 538 ppm for an AFR of λ = 1.45. CH_4, being the predominant contributor to THC emissions, is disclosed separately. THC and CO emissions from natural gas engine operations pose greater interest from a legislative standpoint. THC emissions exceed the legal limit of 1300 mg/m³ (equivalent to approximately 860 ppm) at an AFR of λ = 1.4 and run into the measurement limit of 1000 ppm for leaner combustion. CO, conversely, reaches 1440 mg/m³ at maximum at an AFR of λ = 1.3, its legal limit being 1500 mg/m³. Analog to hydrogen operation, increasing the IMEP reduces fuel slip, lowering CH_4 emissions by 55 ppm per 1-bar increment in IMEP. Comparing NO_x emissions, it is essential to explicitly acknowledge the differences in AFR for natural gas and hydrogen operation, as NO_x are significantly favored with higher combustion temperature. As mean in-cylinder temperatures are not measured, temperatures are derived from simulation, resulting in a maximum of 1612 K in hydrogen and 1771 K in natural gas operation for a respective AFR of λ = 2.5 and λ = 1.5. Figure 10 additionally shows the prolonged high temperatures in natural gas operation, further supporting NO_x formation. This results in NO_x emissions reaching the measurement limit of 1200 ppm at an AFR of λ = 1.4, exceeding the legal limit of 500 mg/m³ by nearly a factor of three. [39, 40]

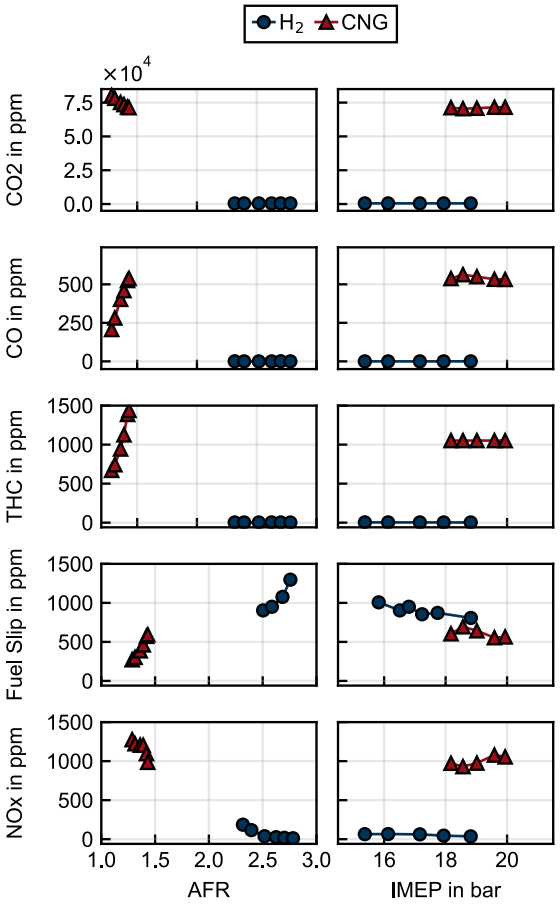

Figure 7: CO_2, CO, THC, NO_x, and the respective fuel slip (H_2 or CH_4) in hydrogen and natural gas operation, varying AFR and IMEP. Data taken from [39]

6 PARTICLE EMISSION

To rule out the influence of particle emissions from intake air pollution, particle numbers were measured in the exhaust and the intake air. The particle emissions from intake air are < 1000 #/cm³

and are, therefore, considered negligible, see Figure 8. The lubrication oil was consistent throughout all operations.

Figure 8 illustrates the influence of engine speed and supercharging level on particle numbers measured in motored operation. PN_{23} and PN_{10} increase with higher engine speeds, and both rise with increased supercharging.

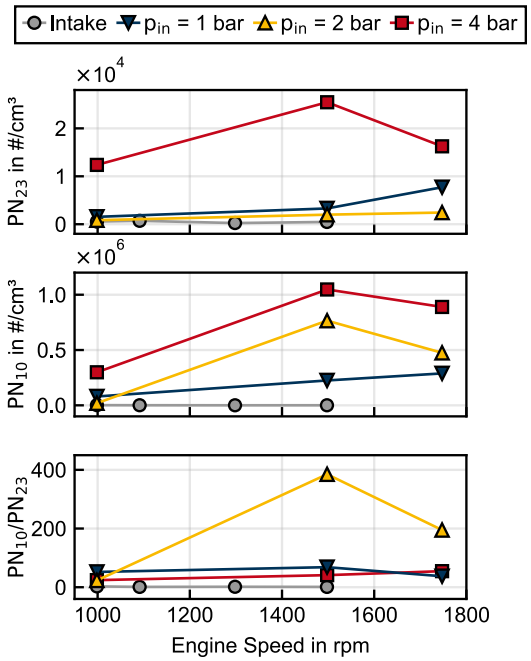

Figure 8: PN_{23}, PN_{10}, and PN_{10}/PN_{23} ratio in motored operation for engine speed and supercharging level (p_{in}) variations. In comparison, particle emissions in the intake air are given. Data taken from [4]

This trend suggests a peak in lubrication oil involvement at the highest supercharging level at the conventional engine speed of 1500 rpm. Furthermore, engine speed significantly influences piston and piston ring friction, contributing to metallic abrasion and subsequent particle emissions associated with engine wear. Comparing motored to fired operation, Figure 9, the overall higher particle numbers in motored operation likely stem from the difference in in-cylinder pressure during the combustion stroke. In-cylinder flow dynamics during load exchange seem to lead to lubrication oil detachment from the liner surface. Additionally, operating the engine with a Miller valve timing – closing the intake valve before the bottom dead center to reduce in-cylinder pressure and temperature – is also assumed to promote particle formation. [4]

Taking a closer look at the fired operation, Figure 9 depicts the influence of variations in AFR and IMEP on PN_{23}, PN_{10}, and PN_{23}/PN_{10}. The measurements of particle emissions are performed analog to measurements of exhaust gas emissions. The AFR varied from λ = 1.4 to 1.7 in steps of 0.05 for natural gas and from λ = 2.5 to 2.9 in steps of 0.10 for hydrogen at an IMEP of 16.5 bar and 15 bar, respectively. Varying the IMEP from 16 to 21 bar in steps of 1 bar for natural gas and from 15 to 17 bar in steps of 0.5 bar for hydrogen operation, the AFR was kept constant at λ = 1.6 and 2.5, respectively. In both variations, the CoC was kept constant at 16 °CA aTDC for natural gas and 10 °CA aTDC for hydrogen. [4]

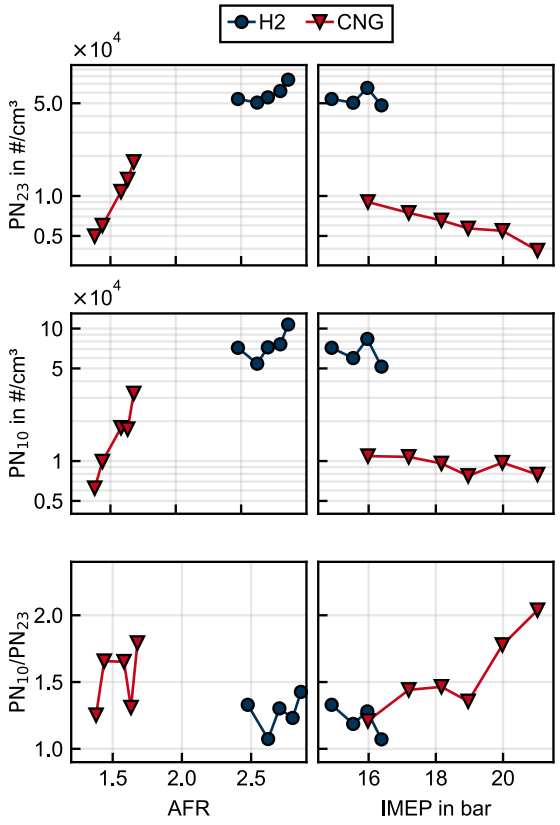

Figure 9: PN_{23}, PN_{10}, and PN_{10}/PN_{23} ratio in hydrogen and natural gas operations for variations of AFR and IMEP. Data taken from [4]

AFR variation impacts particle emissions in both hydrogen and natural gas operations. Leaner combustion increases PN_{23} and PN_{10} in both natural gas and hydrogen operations. This effect is slightly more pronounced for smaller particles, resulting in a higher PN_{10}/PN_{23} ratio for both fuels. In IMEP variation, PN_{23} and PN_{10} decrease with higher IMEP, again in hydrogen and natural gas operations. Unlike in natural gas operation, this affects smaller particles more in hydrogen operation, emphasized in the PN_{10}/PN_{23} ratio. The correlation between AFR or IMEP and particle

emission cannot be attributed to fuel combustion, as the effect is evident even in hydrogen engines, which lack combustion-induced particle emissions. This indicates that oil-derived particles are influenced by in-cylinder temperature, with higher temperatures reducing PN_{23} and PN_{10} emissions, particularly for smaller particles. However, this assumption requires further investigation. Further, as analyzed when comparing motored to fired operations, IMEP variations show an influence of in-cylinder pressure on lubrication oil combustion. [4]

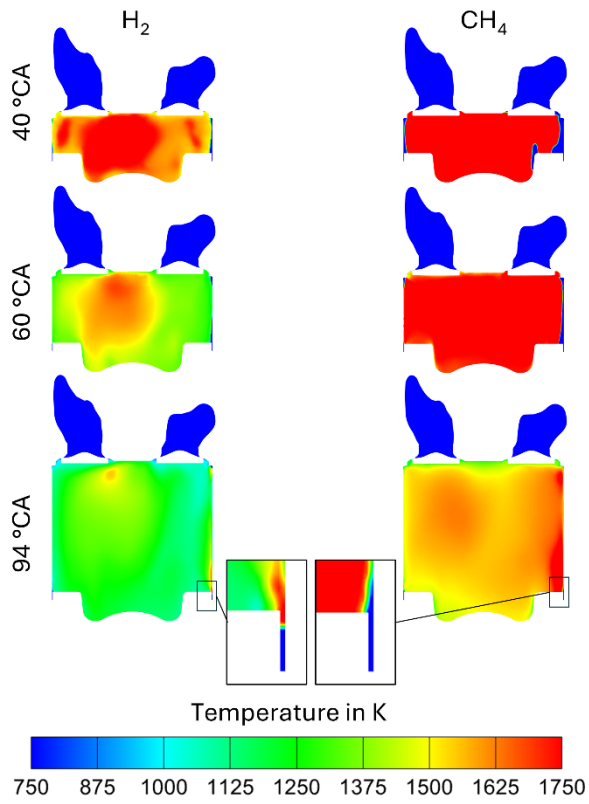

Figure 10: 3D CFD simulation of hydrogen (λ = 2.5) and methane (λ = 1.5) combustion at 1500 rpm comparing flame propagation and flame quenching distance for 40 °CA, 60 °CA, and 94 °CA after TDC

As is known from other alternative fuels like OME, the lack of intramolecular C-C-bonds in fuels significantly inhibits the agglomeration of soot from fuel combustion. This leads to particle numbers lower than $2x10^4$ #/cm³ regarding PN_{23} and lower than $4x10^4$ #/cm³ regarding PN_{10} in natural gas operation. Hydrogen operation results in particle emissions lower than $8x10^4$ #/cm³ regarding PN_{23} and a maximum of $1.5x10^5$ #/cm³ regarding PN_{10} at the lowest IMEP of 15 bar. The slightly higher particle emissions observed during hydrogen operation than natural gas are likely attributed to the increased influence of lubricating oil. This can be due to hydrogen's combustion occurring closer to the combustion chamber wall, resulting in ash particles originating from the oil. As illustrated in Figure 10, simulation results confirm that hydrogen has a shorter flame-quenching distance than methane. The simulations reveal that the hydrogen-air mixture disperses more rapidly within the cylinder, causing the flame to interact with the chamber walls earlier and longer during hydrogen operation than in methane operation. A reference to the exhaust gas measurements can be drawn to evaluate the carbon footprint of lubrication oil involvement in large engines. Unlike natural gas operations, THC, CO, and CO_2 emissions in hydrogen operations fall into the lower measurement limit. [4, 39, 46–51]

7 EXHAUST GAS BACK PRESSURE

Turbocharging is an established technique for enhancing the efficiency of internal combustion engines. By using the otherwise wasted enthalpy of the exhaust gases, turbochargers generate boost pressure exceeding ambient pressure, consequently improving both the thermodynamic and overall system efficiency. However, employing a turbine within the exhaust stream induces back pressure, which impacts in-engine processes. This study experimentally investigates the effects of different exhaust back pressures (EBP) regulated by an exhaust throttle valve and varied between 1.53 and 2.24 bar. The air mass flow is held constant at 550 kg/h and the fuel mass flow at 6.25 kg/h, resulting in an AFR of λ = 2.56. Figure 11 illustrates the cylinder pressures. While the peak pressure reduces as back pressure rises, the pressure during the charge cycle rises with increasing back pressure, leading to a shortened ignition delay (IDT) defined as MFB0-MFB5, as depicted in Figure 12. The ignition delay decreased from 11.16 °CA at 1.53 bar to 10.21 °CA at 2.24 bar. This reduction is attributed to the higher pressures during compression and the associated higher temperatures within the combustion chamber. Conversely, combustion duration (CD), defined as MFB5-MFB95, extends with elevated exhaust back pressure. Inefficient scavenging at higher back pressures results in a higher residual gas content (RGC) within the combustion chamber, thus slowing the combustion process. This phenomenon, coupled with the rising back pressure, contributes to a higher exhaust gas temperature (EGT), which increases from 388 °C to 423 °C. Another consequence of the increased RGC is a more incomplete combustion, exhibiting a higher fuel slip. Fuel slip rises from 553 ppm to 804 ppm as back pressure increases. The slower and less complete combustion at higher back pressures also reduces the effective efficiency (η_e) from 42.3 % to 39.7 %. These findings imply that a turbocharger concept optimized for hydrogen can enhance the efficiency of existing turbocharged

engines. Reducing the exhaust back pressure to 1.53 bar is necessary to maximize the effective efficiency. However, due to the low exhaust gas enthalpy with hydrogen combustion, achieving this reduction would necessitate a turbocharger efficiency (η_T) of 147 %, which is unattainable. Even a reduction to 2.24 bar would demand a turbocharger efficiency of 80 %. The technological limitations of conventional exhaust gas turbochargers highlight the need to explore alternative charging concepts. One potential solution involves employing a compressor to provide the required charge pressure without increasing the exhaust back pressure. Alternatively, an electric turbocharger could be implemented. This approach reduces exhaust back pressure by either electrically assisting the compressor or completely mechanically decoupling the turbine and compressor while still utilizing the exhaust gas enthalpy.

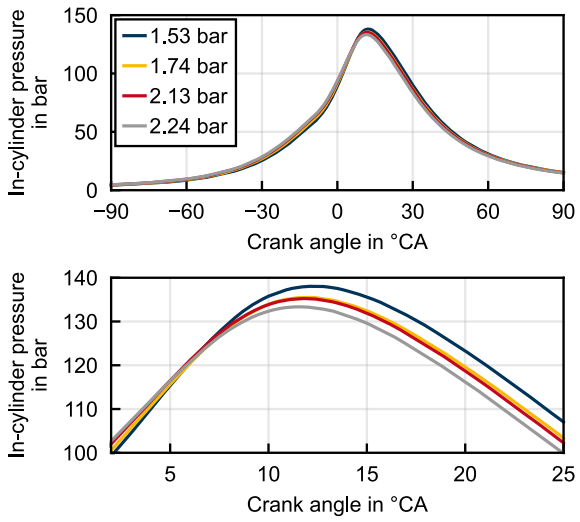

Figure 11: Experimental in-cylinder pressure of different exhaust gas back pressures

Simulations were conducted to investigate the influence of the exhaust gas back pressure beyond the limitations of the experimental setup. In these simulations, the back pressure was varied from 1.5 bar to 4 bar while maintaining a constant boost pressure of 3 bar. This configuration resulted in a varying AFR ranging from λ = 2.30 to 2.54 due to the higher in-cylinder pressures and reduced intake mass flow associated with increased back pressure (Figure 14). The exhaust back pressure significantly influences the in-cylinder pressure (Figure 13). As demonstrated in the experiment, the maximum cylinder pressure decreases with increasing back pressure. This phenomenon arises from the combined effect of a higher AFR and RGC, rising from 0.2 % to 4.2 %. Contrary to the experimental results, where the intake mass flow was held constant, the higher AFR in the simulation results in a higher IDT. The higher RGC for higher back pressures increases the combustion duration, as seen in the experimental setup. This slower combustion arises from the leaner mixture, which reduces flame propagation speed, compounded by the increased RGC, which further dilutes the mixture and lowers combustion temperatures. The combined effects of increased AFR, higher RGC, and combustion duration result in delayed peak pressure and a significant reduction in indicated efficiency.

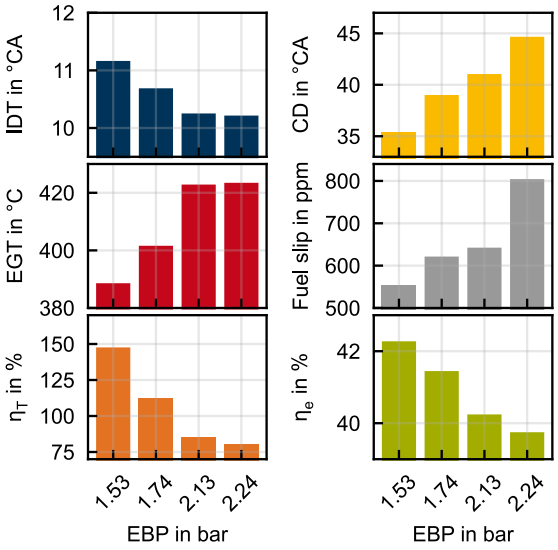

Figure 12: Experimental IDT, CD, EGT, Fuel slip, η_T and η_e of different exhaust gas back pressures

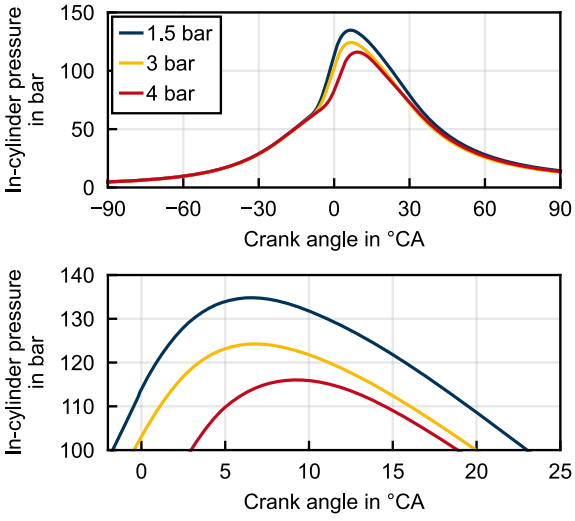

Figure 13: Simulative in-cylinder pressure of different exhaust gas back pressures

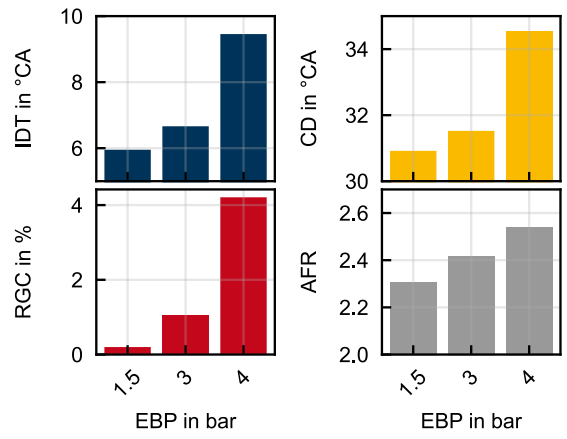

Figure 14: Simulative IDT, CD, RGC, and AFR of different exhaust gas back pressures (1.5 bar, 3 bar, and 4 bar)

Consequently, a high exhaust back pressure significantly reduces the engine's indicated efficiency. This requires the development of alternative turbocharging concepts for hydrogen operation to achieve comparable efficiency levels to natural gas or diesel engines, thereby making hydrogen a viable alternative fuel.

8 SUMMARY AND CONCLUSION

This study allows for an insight into the current research focus on large-scale H2ICEs, thematizing reaction kinematics for hydrogen 3D CFD simulation, exhaust gas composition, temperature, and enthalpy, and suitable turbocharger concepts for H2ICEs by comparing engine performance, combustion behavior, and exhaust gas emissions of a gas engine operated on natural gas and hydrogen. The following findings were made:

- The simulation model built in CONVERGE [21] using the k-ε Reynolds-Averaged Navier-Stokes turbulence model was validated against measurements with a maximum deviation of 2.5 %.

- Four different reaction mechanisms Conv 3.0, Nordin, GRI 3.0, Burke-2012) were investigated and compared against measurements. Conv 3.0 and Nordin provide the most accurate predictions of cylinder pressure. While both mechanisms return similar results, differences arise in the ignition delay time and heat release rate. Conv 3.0 exhibits a shorter ignition delay, whereas Nordin predicts a higher heat release rate. While GRI 3.0 provides acceptable results, it shows a longer ignition delay. Conversely, Burke-2012 significantly overestimates the ignition delay, making it unsuitable for further investigation in this study. Due to its minimal deviations and lowest RMSE, the Conv 3.0 mechanism was selected for further investigation in this study.

- Carbonaceous emissions prove negligible in hydrogen operation concerning emission values complying with German TA Luft regulations. Natural gas operations meanwhile exceed the legal limit of 1300 mg/m^3 for THC emissions (equivalent to approximately 860 ppm) at an AFR of $\lambda = 1.4$ and run into the measurement limit of 1000 ppm for leaner combustion. CO in natural gas operations reaches 1440 mg/m^3 at maximum at an AFR of $\lambda = 1.3$, its legal limit being 1500 mg/m^3.

- CO_2 emissions in hydrogen operation show a constant minimum of 500 ppm, likely due to ambient air, whereby natural gas operation at an AFR of $\lambda = 1.3$ results in 80,170 ppm CO_2.

- The hydrogen engine solely registers significant emission values for NO_x. NO_x emissions significantly rise with richer fuel mixture from 12.0 ppm for an AFR of $\lambda = 2.8$ to 185.5 ppm for an AFR of $\lambda = 2.3$. NO is predominant in NO_x, later oxidizing to NO_2. The peak NO_x emissions are equivalent to 794.6 mg/m^3, momentarily surpassing the 500 mg/m^3 limit. Higher NO_x emissions for richer mixtures result from hydrogen's high adiabatic flame temperature and the rising peak temperatures in the cylinder.

- The fuel slip in hydrogen operation ranges between 800 – 1300 ppm, rising with leaner combustion due to incomplete combustion and reducing with higher IMEP due to a more stable combustion. H_2 emissions are currently not regulated by the German TA Luft regulations.

- Studies on blends of hydrogen or natural gas and conventional fuels to drastically reduce particle emissions in automotive and heavy-duty engines can be confirmed. Fuel-independent particle emissions measured down to 10 nm amount to 10^4-10^5 # cm^{-3}.

- Due to an increased lubrication oil influence in hydrogen operation, the particle emissions in hydrogen operation were slightly higher than in natural gas operation. 3D CFD simulation showed the reduced quenching distance of hydrogen

to the combustion chamber wall and, therefore, interaction with the oil film.

- Higher exhaust back pressure leads to longer combustion duration, incomplete combustion, and reduced engine efficiency due to a higher residual gas content. To reduce exhaust back pressure and maximize efficiency, unrealistically high turbocharger efficiencies would be required. Electric turbochargers or mechanically decoupled systems could minimize exhaust back pressure and increase efficiency. Innovative solutions must be developed to compensate for the disadvantages of higher exhaust back pressure to make hydrogen a competitive fuel.

9 DEFINITIONS, ACRONYMS, ABBREVIATIONS

°CA	Crank Angle Degree
AFR	Air-Fuel Ratio
aTDC	After Top Dead Center
bTDC	Before Top Dead Center
CD	Combustion Duration
CFD	Computational Fluid Dynamic
CHP	Combined Heat and Power
CoC	Center of Combustion
CPC	Condensation Particle Counter
EBP	Exhaust Back Pressure
EGT	Exhaust Gas Temperature
H2ICE	Hydrogen Internal Combustion Engine
IDT	Ignition Delay
MFB*x*	Mass Fraction Burned *x* %
p_{in}	Supercharging Level
PISO	Pressure Implicit with Splitting of Operators
ppm	Parts per Million
RGC	Residual Gas Content
rpm	Rounds per Minute
TDC	Top Dead Center
THC	Total Hydrocarbons
η_T	Effective Efficiency
η_e	Turbocharger Efficiency

10 CONTACT

Andreas Zepf, corresponding author
Institute of Sustainable Mobile Powertrains
Technical University of Munich
Schragenhofstraße 31, 80992 Munich, Germany
andreas.zepf@tum.de

11 ACKNOWLEDGEMENTS

Convergent Science provided CONVERGE licenses and technical support for this work.

12 REFERENCES

[1] United Nations, 2023, The Sustainable Development Goals Report 2023: Special Edition, *Department of Economic and Social Affairs*.

[2] IEA, Global EV Outlook 2023, vol. 2023. [Online]. Available: iea.org/reports/global-ev-outlook-2023

[3] Cornet, A. *et al.*, 2021, Why the automotive future is electric: Mainstream EVs will transform the automotive industry and help decarbonize the planet, *McKinsey & Company.* [Online]. Available: mckinsey.com/industries/automotive-and-assembly/our-insights/why-the-automotive-future-is-electric#/

[4] Armbruster, F., Gelner, A., Zepf, A., Prager, M., Härtl, M., and Jaensch, M., 2024, Investigations on particle emissions of large-bore engines powered by natural gas and hydrogen, *Environ. Sci.: Adv.*, vol. 3, no. 11, pp. 1524–1536, doi: 10.1039/d4va00200h.

[5] Schemme, S., Samsun, R. C., Peters, R., and Stolten, D., 2017, Power-to-fuel as a key to sustainable transport systems – An analysis of diesel fuels produced from CO 2 and renewable electricity, *Fuel*, vol. 205, pp. 198–221, doi: 10.1016/j.fuel.2017.05.061.

[6] Wulf, C., Linßen, J., and Zapp, P., 2018, Review of Power-to-Gas Projects in Europe, *Energy Procedia*, vol. 155, pp. 367–378, doi: 10.1016/j.egypro.2018.11.041.

[7] Welder, L. *et al.*, 2019, Design and evaluation of hydrogen electricity reconversion pathways in national energy systems using spatially and temporally resolved energy system optimization, *International Journal of Hydrogen Energy*, vol. 44, no. 19, pp. 9594–9607, doi: 10.1016/j.ijhydene.2018.11.194.

[8] Wróbel, K., Wróbel, J., Tokarz, W., Lach, J., Podsadni, K., and Czerwiński, A., 2022, Hydrogen Internal Combustion Engine Vehicles: A Review, *Energies*, vol. 15, no. 23, p. 8937, doi: 10.3390/en15238937.

[9] Boretti, A., 2020, Hydrogen internal combustion engines to 2030, *International Journal of Hydrogen Energy*, vol. 45, no. 43, pp. 23692–23703, doi: 10.1016/j.ijhydene.2020.06.022.

[10] Santangelo, P. E. and Tartarini, P., 2007, Fuel cell systems and traditional technologies. Part I: Experimental CHP approach, *Applied Thermal Engineering*, vol. 27, 8-9, pp. 1278–1284, doi: 10.1016/j.applthermaleng.2006.11.002.

[11] Yu, S. *et al.*, 2023, Hydrogen-based combined heat and power systems: A review of technologies and challenges, *International Journal of Hydrogen Energy*, vol. 48, no. 89, pp. 34906–34929, doi: 10.1016/j.ijhydene.2023.05.187.

[12] Environmental Protection Agency, *CHP's Role in a Decarbonizing Energy Grid: CHP Benefits.* [Online]. Available: www.epa.gov / chp/chp-benefits (accessed: Dec. 29 2024).

[13] Rolls Royce Solutions, *Energy transition: Rolls-Royce reaches milestone with H2-ready certificate for mtu engines.* [Online]. Available: www.rolls-royce.com/ media/press-releases/2024/11-7-2024-energy-transition-rr-reaches-milestone-with-h2-ready-certificate-for-mtu-engines.aspx (accessed: Dec. 29 2024).

[14] MAN Energy Solutions, *H2-ready: MAN-Gasmotoren ermöglichen Wasserstoffeinsatz in Kraftwerken.* [Online]. Available: www.man-es.com/docs/default-source/press-releases-new/20211104_man_es_pm_h2-ready_gasmotoren_de.pdf?sfvrsn=17e15339_2 (accessed: Dec. 29 2024).

[15] INNIO Jenbacher GmbH & Co OG, *Hydrogen: Investing in a Green Future.* [Online]. Available: www.innio.com/en/m?task=read&file=o_media_file_en&id=3526 (accessed: Dec. 29 2024).

[16] Wärtsilä Energy, *Wärtsilä launches world's first large-scale 100% hydrogen-ready engine power plant.* [Online]. Available: www.wartsila.com/media/news/18-06-2024-wartsila-launches-world-s-first-large-scale-100-hydrogen-ready-engine-power-plant-3464281 (accessed: Dec. 29 2024).

[17] Caterpiller Inc., *Powering Sustainability: Renewable Hydrogen Power Solutions.* [Online]. Available: www.cat.com/en_GB/by-industry/electric-power/electric-power-industries/hydrogen.html (accessed: Dec. 29 2024).

[18] Liquon Schmierstoff GmbH, Sentron: Motorenöle für stationäre Gasmotoren. [Online]. Available: liquon.com/petro-canada-sentron-ld-8000/15017880

[19] Liquon Schmierstoff GmbH, 2022, Sentron LD 8000: Premium Motorenöl für station ¨ are Gasmotoren. [Online]. Available: liquon.com/petro-canada-sentron-ld-8000/15017880

[20] Stark, M., Kraus, C., Fellner, F., and Jaensch, M., 2024, Combined exhaust gas and optical investigation of methanol DI-engine with focus on the fuel spray-wall interaction, *International Journal of Engine Research*, vol. 25, no. 10, pp. 1801–1817, doi: 10.1177/14680874241252455.

[21] Richards, K. J., Senecal, P. K., and Pomraning, E., *CONVERGE 3.0*. Madison, WI: Convergent Science, 2024.

[22] Senecal, P. K. *et al.,* Multi-Dimensional Modeling of Direct-Injection Diesel Spray Liquid Length and Flame Lift-off Length using CFD and Parallel Detailed Chemistry in *SAE Technical Paper Series*, 2003.

[23] Richards, K. J., Senecal, P. K., and Pomraning, E., 2021, CONVERGE 3.0 Manual, *Convergent Science*.

[24] Issa, R., 1986, Solution of the implicitly discretised fluid flow equations by operator-splitting, *Journal of Computational Physics*, vol. 62, no. 1, pp. 40–65, doi: 10.1016/0021-9991(86)90099-9.

[25] Knop, V., Benkenida, A., Jay, S., and Colin, O., 2008, Modelling of combustion and nitrogen oxide formation in hydrogen-fuelled internal combustion engines within a 3D CFD code, *International Journal of Hydrogen Energy*, vol. 33, no. 19, pp. 5083–5097, doi: 10.1016/j.ijhydene.2008.06.027.

[26] Kéromnès, A. *et al.*, 2013, An experimental and detailed chemical kinetic modeling study of hydrogen and syngas mixture oxidation at elevated pressures, *Combustion and Flame*, vol. 160, no. 6, pp. 995–1011, doi: 10.1016/j.combustflame.2013.01.001.

[27] Hu, E., Pan, L., Gao, Z., Lu, X., Meng, X., and Huang, Z., 2016, Shock tube study on ignition delay of hydrogen and evaluation of various kinetic models, *International Journal of Hydrogen Energy*, vol. 41, no. 30, pp. 13261–13280, doi: 10.1016/j.ijhydene.2016.05.118.

[28] Ó Conaire, M., Curran, H. J., Simmie, J. M., Pitz, W. J., and Westbrook, C. K., 2004, A comprehensive modeling study of hydrogen oxidation, *Int J of Chemical Kinetics*, vol. 36, no. 11, pp. 603–622, doi: 10.1002/kin.20036.

[29] Li, J., Zhao, Z., Kazakov, A., and Dryer, F. L., 2004, An updated comprehensive kinetic model of hydrogen combustion, *Int J of Chemical Kinetics*, vol. 36, no. 10, pp. 566–575, doi: 10.1002/kin.20026.

[30] Mueller, M. A., Kim, T. J., Yetter, R. A., and Dryer, F. L., 1999, Flow reactor studies and kinetic modeling of the H2/O2 reaction, *Int J of Chemical Kinetics*, vol. 31, no. 2, pp. 113–125, doi: 10.1002/(SICI)1097-4601(1999)31:2<113::AID-KIN5>3.0.CO;2-0.

[31] G. P. Smith *et al., GRI-MECH 3.0.* [Online]. Available: www.me.berkeley.edu/gri_mech/ (accessed: Dec. 22 2024).

[32] Davis, S. G., Joshi, A. V., Wang, H., and Egolfopoulos, F., 2005, An optimized kinetic model of H2/CO combustion, *Proceedings of the Combustion Institute*, vol. 30, no. 1, pp. 1283–1292, doi: 10.1016/j.proci.2004.08.252.

[33] Saxena, P. and Williams, F. A., 2006, Testing a small detailed chemical-kinetic mechanism for the combustion of hydrogen and carbon monoxide, *Combustion and Flame*, vol. 145, 1-2, pp. 316–323, doi: 10.1016/j.combustflame.2005.10.004.

[34] Konnov, A. A., 2008, Remaining uncertainties in the kinetic mechanism of hydrogen combustion, *Combustion and Flame*, vol. 152, no. 4, pp. 507–528, doi: 10.1016/j.combustflame.2007.10.024.

[35] Burke, M. P., Chaos, M., Ju, Y., Dryer, F. L., and Klippenstein, S. J., 2012, Comprehensive H 2 /O 2 kinetic model for high-pressure combustion, *Int J of Chemical Kinetics*, vol. 44, no. 7, pp. 444–474, doi: 10.1002/kin.20603.

[36] Hong, Z., Davidson, D. F., and Hanson, R. K., 2011, An improved H2/O2 mechanism based on recent shock tube/laser absorption measurements, *Combustion and Flame*, vol. 158, no. 4, pp. 633–644, doi: 10.1016/j.combustflame.2010.10.002.

[37] Varga, T. *et al.*, 2015, Optimization of a hydrogen combustion mechanism using both direct and indirect measurements, *Proceedings of the Combustion Institute*, vol. 35, no. 1, pp. 589–596, doi: 10.1016/j.proci.2014.06.071.

[38] Nordin, N., Numerical Simulations of Non-Steady Spray Combustion Using a Detailed Chemistry Approach, Dept. of Thermo and Fluid Dynamics, Chalmers University of Technology, Göteborg, Sweden.

[39] Armbruster, F., Kraus, C., Prager, M., Härtl, M., and Jaensch, M., 2024, Optimized Emission Analysis in Hydrogen Internal Combustion Engines: Fourier Transform Infrared Spectroscopy Innovations and Exhaust Humidity Analysis, *SAE Int. J. Engines*, 17 (7), doi: 10.4271/03-17-07-0052.

[40] Bundesregierung, Neufassung der Ersten Allgemeinen Verwaltungsvorschrift zum Bundes-Immissionsschutzgesetz: (Technische Anleitung zur Reinhaltung der Luft – TA Luft) GMBl 2021 Nr. 48-54, S. 1050, Aug. 2021. Accessed: Aug. 18 2023.

[41] Global Monitoring Laboratory, *Carbon Cycle Greenhouse Gases: Trends in Atmospheric Carbon Dioxide.* [Online]. Available: gml.noaa.gov/ccgg/trends/ (accessed: Dec. 22 2023).

[42] Verhelst, S. and Wallner, T., 2009, Hydrogen-fueled internal combustion engines, *Progress in Energy and Combustion Science*, vol. 35, no. 6, pp. 490–527, doi: 10.1016/j.pecs.2009.08.001.

[43] G. P. Merker and R. Teichmann, Eds., *Grundlagen Verbrennungsmotoren: Funnktionsweise und alternative Antriebssysteme Verbrennung, Messtechnik und Simulation*. Wiesbaden: Springer Fachmedien Wiesbaden, 2019.

[44] Eichlseder, H. and Klell, M., *Wasserstoff in der Fahrzeugtechnik: Erzeugung, Speicherung, Anwendung,* 2nd ed. Wiesbaden: Vieweg+Teubner, 2010.

[45] Nuttall, W. J. and Bakenne, A. T., *Fossil Fuel Hydrogen*. Cham: Springer International Publishing, 2020.

[46] Härtl, M., Seidenspinner, P., Wachtmeister, G., and Jacob, E., 2014, Synthetic Diesel

Fuel OME1 A Pathway Out of the Soot-NOx Trade-Off, *MTZ Worldw*, vol. 75, 7-8, pp. 48–53, doi: 10.1007/s38313-014-0173-1.

[47] Gelner, A. D. *et al.*, 2022, Gaseous emissions of a heavy-duty engine fueled with polyoxymethylene dimethyl ethers (OME) in transient cold-start operation and methods for after-treatment system heating, *Environ. Sci.: Adv.*, vol. 1, no. 4, pp. 470–482, doi: 10.1039/d2va00080f.

[48] Gelner, A. D. *et al.*, 2022, Gaseous emissions of a heavy-duty engine fueled with polyoxymethylene dimethyl ethers (OME) in transient cold-start operation and methods for after-treatment system heating, *Environ. Sci.: Adv.*, vol. 1, no. 4, pp. 470–482, doi: 10.1039/d2va00080f.

[49] N. Beishuizen, D. Mayer, and D. Efimov, *Quenching and flash-back of hydrogen flames on perforated plate burners* (accessed: Jun. 4 2024).

[50] Benim, A. C. and Pfeiffelmann, B., 2019, Prediction of burning velocity and quenching distance of hydrogen flames, *E3S Web Conf.*, vol. 128, p. 1012, doi: 10.1051/e3sconf/201912801012.

[51] Movileanu, C., Mitu, M., Giurcan, V., Razus, D., and Oancea, D., 2020, Quenching distances, minimum ignition energies and related properties of propane-air-diluent mixtures, *Fuel*, vol. 274, p. 117836, doi: 10.1016/j.fuel.2020.117836.